

Structure and Activity of Potential-Dependent Pt(110) Surface Phases Revealed from Machine-Learning Atomic Simulation

Published as part of *The Journal of Physical Chemistry virtual special issue "125 Years of The Journal of Physical Chemistry"*.

Ya-Hui Fang,* Dan-dan Song, Hui-xia Li, and Zhi-Pan Liu*

Cite This: <https://doi.org/10.1021/acs.jpcc.1c02222>

Read Online

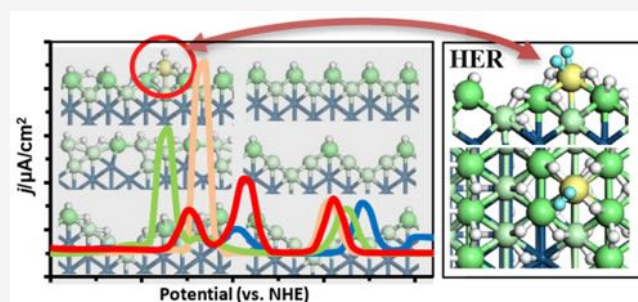
ACCESS |

Metrics & More

Article Recommendations

Supporting Information

ABSTRACT: Electrodes can undergo significant surface structure reconstruction under electrochemical conditions, which in turn significantly affects its electrochemical performance. This complex phenomenon raises continuous interests in both science and industry for understanding the structure–activity dynamics under electrochemical conditions. Here we report the first theoretical attempt, by combining the machine-learning-based global optimization (SSW-NN method) and modified Poisson–Boltzmann continuum solvation (CM-MPB) based on first-principles calculations, to elucidate the potential-dependent structure evolution on a stepped Pt surface and its catalytic activity, in which the cyclic voltammetry (CV) curves are simulated to compare with experiment. We selected four types of structure domains on Pt(110), namely, Type-Ia: ordered Pt(110)-(1 × 1); Type-Ib: disordering of Pt(110)-(1 × 1); Type-II: ordered Pt(110)-(1 × 2) (the missing-row reconstruction); and Type-III: reconstructed Pt(110)-(1 × 4), and reveal the potential dependence of the coverage of H atom adsorbate, the total passed charge, and the CV of these Pt(110) surface domains. In particular, the surface reconstruction from Type-Ia to -Ib occurs at +0.20 V vs NHE when the average H coverage is above 0.60 ML, which produces the key five-coordinated Pt (Pt_{5c}) sites. The Pt_{5c} sites exhibit the superior activity for hydrogen evolution reaction (HER) and are the key species responsible for the high HER activity of Pt electrode.



1. INTRODUCTION

Potential-induced electrode surface reconstruction occurs commonly in electrochemistry and has a vital impact on the electrode performance (e.g., efficiency, selectivity and stability).^{1–3} The platinum electrode as an indispensable material for fuel cell application,^{4–7} and it has long been observed that the hydrogen adsorption/desorption process is structure-sensitive according to macroscopic cyclic voltammetry (CV),^{8,9} which further regulates the electrocatalytic reactions, such as the hydrogen evolution/oxidation reaction (HER/HOR)^{8,10,11} and CO₂ reduction reaction (CO₂RR).^{12,13} It was thus a long-standing challenge to probe the atomic structure at the adlayer/solution/electrode interface in order to shed light on the potential-induced interface dynamics and their impact on catalytic reactivity.

The electrochemical hydrogen adsorption on a Pt electrode has been intensely studied in history. Previous experiment studies showed that Pt(110) is the most active crystal plane for catalytic HER, and the catalytic activity can be effectively increased with more (110) exposed.^{8,14–17} This has inspired detailed studies on the interaction of adsorbates on Pt(110) electrode^{16,18–20} at different potential ranges, particularly, in

the underpotential (H_{upd}) region (0.05–0.4 V, RHE), where different H adsorbate coverages are present with no HER interference. Different CV curves of (110) have, however, been recorded, and they appear to be dependent on the cooling condition after flame annealing, namely, hydrogen-cooled and CO-cooled electrodes. From the surface science knowledge, the different behaviors of Pt(110) CVs were suspected to be due to the varied populations of (1 × 1) and (1 × 2) domains ((1 × 2) is a typical missing row reconstruction of (1 × 1) under surface science conditions).²¹ For hydrogen cooled electrode, the CV at the H_{upd} region shows two peaks at 0.12 and 0.25 V vs RHE, which should be related to the missing row (1 × 2) structure reconstruction since it was indeed observed by using in situ Fourier transform infrared technique and CV.^{22–24} However, multiple reversible electroadsorption peaks

Received: March 11, 2021

Revised: April 29, 2021

centered at 0.145, 0.20, and 0.25 V vs RHE for the CO-cooled electrode are not assigned properly due to the appearance of the additional 0.20 V peak, where the surface is initially dominated by the (1 × 1) surface domain.^{23,25,26} To clarify the experiment, an atomic level knowledge of the electrode is required, which involves complex hydrogen adsorption/desorption states at different local atomic structures, such as terraces,²⁷ steps,²² and reconstructed sites^{20,28} and the sites with coadsorption of anion and cation.^{23,25}

As the catalyst with the highest HER activity under acidic conditions, the active site of Pt electrode has been actively investigated for years. It was observed that the ridged (110) surface is always more active (ca. 2 times) for HER/HOR than are the (111) and (100) terraces.^{8,14–17} The Tafel slope of Pt(110) (~28 mV/dec) is smaller than the (111) and (100) (~40–120 mV/dec) surfaces, which means that the Tafel reaction is the key step of HER on Pt(110). In accordance with this, Hoshi's group found that the exchange current density (j_0) increases linearly with the increase of the step and concluded that the stepped sites are the active site of HER/HOR.^{29–31} On going to nanoparticles in real catalysts, the catalytic activity can be influenced by many factors, including the size, facets, edges, and corners of nanoparticles, and there is no consensus on the active site from experiments.^{2,32–34} The recent advance in theoretical calculation^{35–42} has provided a powerful way to understand the activity at the atomic level. Importantly, these calculations suggested that the bulk-truncated Pt surfaces in fact do not have the high activity: At the typical surface coverage at 0 V vs NHE, namely, ~1 monolayer (ML) of H, the barrier of HER/HOR calculated is generally high (e.g., above 0.7 eV on the Pt(111), Pt(100), and Pt(110) surfaces).^{43–46} However, Wei et al. have identified the active site of a small Pt₄₄ octahedron particle to be the apex atoms (five- or six-coordinated Pt atoms shared by at least three facets), which has a low H–H coupling barrier of ~0.48 eV.⁴⁷ The activity at these low-coordinated Pt sites is higher than those at terraces (111) and (100) sites of the particle.¹¹ It is naturally expected that extensive Pt surfaces should also contain such active Pt sites under electrochemical conditions, possibly due to the surface reconstruction, but how to determine the reconstructed surface structure under electrochemical conditions remains a key problem in the field, which we need to take into account at least the adsorbate coverage, the surface structure dynamics, and the varied potential.

Herein we aim to understand why the CV curve of Pt(110) surface is structure-sensitive and how it affects the HER activity. By using machine-learning atomic simulation, we have mapped out the low-energy structures of Pt(110) under electrochemical conditions. In particular, a facile reconstruction is identified on the ordered Pt(110)-(1 × 1) at 0.60 ML average H coverage that leads to the appearance of the five-coordinated Pt_{5c} sites. This reconstruction can be correlated with the 0.20 V peak that appears in the CO-cooled electrode CV curve in experiment. Our results disentangle the roles of the electrode pretreatment and the electrochemical potentials on reconstructing the electrode surface structure and on changing the HER activity. The high activity of Pt(110) is now clarified by correlating the HER rate with the surface Pt_{5c} sites.

2. METHODS

The SSW-NN method^{48–52} is used for fast global structure search by combining the global neural network (G-NN) potential with the stochastic surface walking (SSW) global

optimization method. With SSW-NN simulation, one can routinely search for 10⁷ structures on global PES for systems up to 200 atoms per cell and cover all likely coverages. The detail of the method and the calculation setup have been described in recent publications.⁵² The G-NN potential is generated by iterative self-learning of the DFT global PES data set generated from SSW exploration, which contains three steps: (i) global data set generation based on DFT calculations using selected structures from SSW simulation, (ii) G-NN potential fitting, and (iii) SSW global optimization using G-NN potential. These three steps are iteratively performed until the G-NN potential is transferable and robust enough to describe the global PES. Then the Bayesian optimization algorithm is utilized to guide the SSW-NN global PES search (Bayesian-SSW-NN) for selected H_{*θ*}/Pt (the coverage θ_i defined as the $x_{\text{adsorbed_H_atoms}}/n_{\text{surface_atoms}}$) systems to guarantee the correct global minima (GM) configuration being obtained.

For the Pt(110) surfaces, we utilized $p(3 \times 4)$ (24 atoms per layer) six-layer slabs with adsorbates on both sides of the surfaces. The solid–liquid interface was described using the periodic continuum solvation model based on the modified Poisson–Boltzmann equation (CM-MPB), which can take into account the solvation and potential effect.^{45,53,54} The charged-slab DFT/CM-MPB method developed previously^{53–55} is utilized to add explicit charge onto the surface, and a neutralizing countercharge is added into solvation following the MPB equation. The addition of excess surface charge will shift the electrochemical potential of system (the potential difference between Fermi level and the potential in solution) and thus can be determined explicitly via DFT/CM-MPB method. It should be mentioned that DFT calculations have been utilized to validate the low energy structures and confirm the identified global minimum. All energetics reported in this work are from DFT without specifically mentioning. The other calculation details on SSW and DFT calculation setups can also be found in the [Supporting Information](#).

3. RESULTS

3.1. Surface Phases and the Related CV Curves. To study the potential-dependent surface phases and the possible adsorbed-induced reconstruction, it is essential to identify the low energy phases under electrochemical potentials, which needs to determine the coverage of adsorbates on surface at different potentials. In this work, we consider the possibility of the surface structure reconstruction with the help of machine-learning atomic simulation. We utilize SSW-NN global optimization to explore extensively the surface coverage of H at a series of adsorbed H atoms (θ_i), i.e. $x/24$ ML with $x = 1, 2, 3, \dots, 25$ hydrogen atoms on Pt(110) with different surface geometries (domain). For each phase (θ_i), defined by a certain H coverage (θ_i) on a surface domain (t) with a particular surface geometry (i.e., Pt coordinates), the thermodynamics stability can be evaluated by computing the reaction free energy in eq 1, where the H on surface is treated to be in equilibrium ($\text{H}^+ + \text{e}^- \leftrightarrow \text{H}^*(\theta_i)$) with the solvated proton in solution.

$$\Delta G_{\theta_i}(U) = G(\theta_i) - G_{\text{sur}} - \frac{\theta_i}{2} G_{\text{H}_2} - eU \quad (1)$$

Equation 1 shows the reaction free energy of phase θ_i is dependent on the potentials (U), where $G(\theta_i)$ is the Gibbs free

energy of H adsorbed surface at the coverage θ_i where the vibrational zero-point energy for adsorbed H atoms has been taken into account, and G_{sur} is the Gibbs free energy of the clean surface (approximated by DFT total energy since the entropy effects are negligibly small for solid states). From our previous studies and others work,^{45,56} the reaction free energy can be evaluated based on neutral slab calculations, which is accurate enough for determining the phase diagram. Furthermore, the population of a phase at U , is obtained from eq 2 based on Boltzmann distribution. Finally, the average H coverage ($\theta_i^a(U)$) of this particular surface domain t at the potential U can be derived by summing up the contribution from all the possible phases (eq 3). By using eqs 1–3, the surface phase–potential diagrams can be determined. It is shown that the $\theta_i^a(U)$ at certain potential is determined by the several key coverages (θ_i) based on the Boltzmann distribution. Taking the Pt(110-(1 × 1) surface as example, the average H coverage at 0.2 V is about 0.60 ML (Figure 2a), which is mainly contributed by the 0.5 ML ($x_{0.5} = 27.64\%$) to 0.67 ML ($x_{0.67} = 47.62\%$) adsorbed hydrogen. For the detailed analysis in the following, the dominated high coverage at certain potential has been selected for simplicity. The calculated phase diagrams further enable us to evaluate the total passed charge and the related voltammetric curves at underpotential deposition (H_{upd}) region.

$$x_i(U) = e^{-\Delta G_{q_i}(U)/RT} / \sum_i e^{-\Delta G_{q_i}(U)/RT} \quad (2)$$

$$\theta_i^a(U) = \sum_i (\theta_i(U) \times x_i(U)) \quad (3)$$

In order to obtain the CV curves, we need to first compute the total passed charge ($Q_t(U)$) using eq 4 by summing the passed charge of all phases due to discharging, where n refers to the discharge (e) number of protons to adsorbed H atoms on surface. The current ($j_t(U)/(\mu\text{A}/\text{cm}^2)$) in eq 5 can then be computed by differentiating total passed charge versus time.⁵⁷

$$Q_t(U) = \sum_i n e \times (\theta_i(U) \times x_i(U)) \quad (4)$$

$$j_t(U) = \frac{dQ_t(U)}{dt} = \frac{dQ_t(U)}{dU} \times \frac{dU}{dt} = \frac{dQ_t(U)}{dU} \times \nu \quad (5)$$

Since the total passed charge is closely related to the electrochemical potential, we can equally rewrite the derivation with respect to potential, and obtain eq 5 by relating to the sweep rate ν (set as 50 mV/s), that is, $\frac{dU}{dt}$. It is thus possible to calculate the CV curves based on the total passed charge and related potential by eq 5. The expectation value of the properties of the whole electrode, including the overall coverage, total passed charge and current ($X(U)$, $X = \theta$, Q , and j) can be finally calculated by adding the contribution of all the likely surface domains (t) as shown in eq 6, where the c_t is the proportions of the domain t . The value of c_t is related to many factors that can reconstruct the surface, including the experimental pretreatment condition and the electrochemical potentials.

$$X(U) = \sum_t c_t X_j(U) \quad (X = \theta, Q, \text{ and } j) \quad (6)$$

In this work, by using SSW-NN we identified four low energy surface structures at the potential range 0–0.4 V, namely, Type-Ia, -Ib, -II, and -III, which can be classified into three different domains from Type-I to -III. Type-Ia and -Ib belong to the same domain due to the small difference in the surface structure, and the transformation between Type-Ia and -Ib is kinetically facile (see section 3). The side and top view of these surface structures are shown in Figure 1 (see also Figures S1–S4). In the following, we describe the structure and stability of them at two representative potentials (i.e., 0.2 and 0 V) as shown in Figure 1.

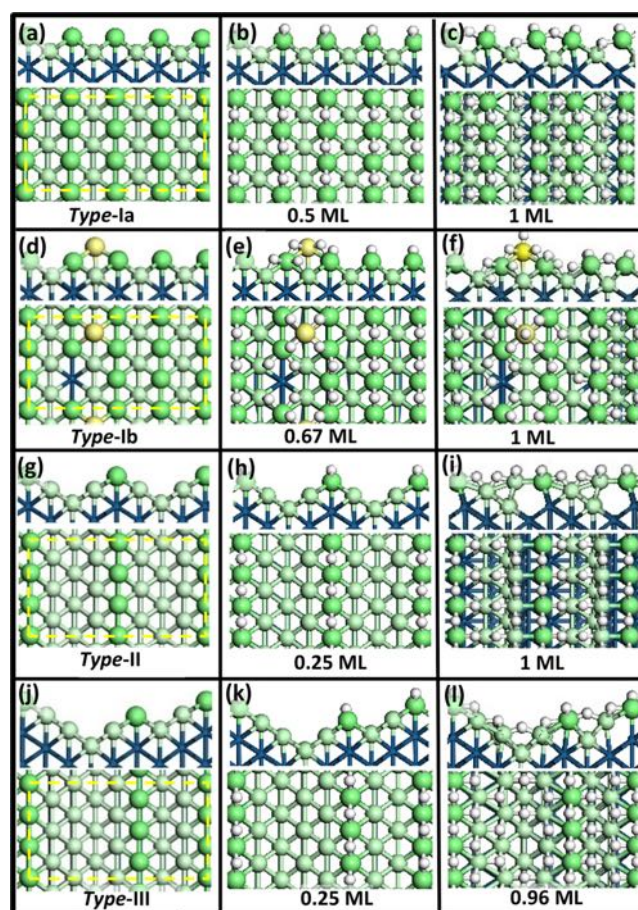


Figure 1. Side and top view of Type-Ia (a–c), Type-Ib (d–f), Type-II (g–i) and Type-III (j–l) surfaces. The first (a, d, g, and j) column refers to the clean surface structures, the middle (b, e, h, and k) and third column (c, f, i, and l) refer to the optimized structure of the four Type surfaces at about 0.2 and 0 V, respectively. Large green ball: surface bridge Pt atoms; large pale green ball: surface terrace Pt atoms; large yellow ball: five-coordinated Pt; small white ball: H atoms.

3.1.1. Type-Ia (Ordered (1 × 1) Domain). The ordered (1 × 1) surface pattern of Pt(110) can be directly truncated from Pt bulk. It comprises ridge sites and narrow terrace sites (Figure 1a). The ridge sites are preferentially occupied by bridging H (see Figure 1b) at about +0.2 V vs NHE. The H atoms will then occupy the vacancy bridge and terrace sites (3-fold hollow sites) at lower potentials and thus weaken the ridge Pt with the underneath surface. At 0 V, we notice that the ridge Pt atoms are pushed outward substantially (>0.4 Å comparing to its bulk truncated position), as shown in Figure 1c.

3.1.2. Type-Ib (Disordering of (1×1) Domain). Type-Ib surface differs from Type-Ia, in that a small fraction of the surface ridge Pt atoms move onto the neighbor valley, forming five-coordinated Pt (Pt_{5c}) sites (Figure 1d). This causes the disordering of the (1×1) domain. Each Pt_{5c} is in a pyramidal geometry bonding with four nearby ridge Pt atoms and one underneath Pt. At 0.2 V, the Pt_{5c} atom is stabilized by coordination with four hydrogen atoms. With the decrease of potential, the H atom can further adsorb on the top site of Pt_{5c} atom, forming a $[\text{PtH}_5]$ local coordination. At 0 V (as shown in Figure 1f), the exposed Pt_{5c} and ridge Pt are all blocked by adsorbed H.

It should be mentioned that the surface disordering from Type-Ia to Type-Ib is identified from SSW global optimization at high average H coverage conditions, suggesting that the surface structure reconstruction is driven by thermodynamics. This critical average H coverage is 0.60 ML, which corresponds to about 0.2 V: Type-Ib is thus more stable below 0.2 V and changes to Type-Ia above 0.2 V. The disordering creates more low-coordinated Pt sites for H atom adsorption and decrease the repulsive interaction between adsorbed H, which is evident by the increase of the free energy gain at the same H coverage: For example, as shown by eq 7, the differential free energy adsorption $\Delta G_{\theta_i}^{\text{diff}}$ (eq 7) for Type-Ia and -Ib surfaces at 0.67 ML H coverage are -0.05 and -0.24 eV, respectively. Obviously, although the Pt_{5c} has less coordination with surface Pt, it can bond with up to five H atoms and thus the reconstruction with Pt migration is overall energetically favorable at low potentials.

$$\Delta G_{\theta_i}^{\text{diff}}(U) = \Delta G_{\theta_i}(U) - \Delta G_{\theta_{i-1}}(U) \quad (7)$$

3.1.3. Type-II (Ordered (1×2) Domain). This is the surface commonly known as the missing-row reconstructed Pt(110)- (1×2) surface, where the ridge sites are separated by the wider (111) valleys. Similarly, H atoms already start to adsorb on the ridge sites at the high potentials (>0.2 V), as shown in Figure 1h. The H atoms then adsorb at the 3-fold terrace hollow sites at the lower potentials. At the high H coverage condition of 0 V, our SSW optimization found that the terrace Pt atoms start to move out from the surface plane toward the valley. As illustrated in Figure 1i, these Pt atoms basically breaks the original Pt–Pt bond by increasing the distance from 2.81 to 3.90 Å, and the Pt atoms at the valley form a (100)-like local pattern.

3.1.4. Type-III (Reconstructed (1×4) Domain). Our SSW global optimization also identifies a reconstructed Pt(110)- (1×4) surface domain, as shown in Figure 1j, where the reconstruction creates steps and wider (111) terraces that form a large valley. There are two types of low-coordinated sites, namely, the original ridge sites (Pt_{ridge}) and the stepped Pt (Pt_{steps}) sites, as indicated in Figure 1j. Similar to other surfaces, the ridge and stepped sites are preferentially occupied by adsorbed H atoms at 0.2 V (Figure 1k). At lower potential (0 V), the H atoms will adsorb at the terrace hollow sites as shown in Figure 1l.

According to our results in determined H adsorbed structures, it is noticed the surface structure is closely related to H adsorption energy. To compare with the stability of the surface H phases, we have listed the hydrogen adsorption energy ($\Delta G_{\theta_i}(U)$ per (1×1)) (eq 1)) at potentials about 0.3, 0.2, and 0 V in Table 1, where the G_{sur} in eq 1 is set as the clean Type-I surface. Our results showed that the Type-II and

Table 1. Adsorption Free Energy (ΔG_{θ_i} per (1×1)) at 0.3, 0.2, and 0 V for Different Pt(110) Surfaces^a

surface	θ_i/ML	$\Delta G_{\theta_i}/\text{eV}$		
		0.3 V	0.2 V	0 V
Type-I	0.5	-0.08	-0.18	-0.38
	0.67	-0.05	-0.18	-0.46
	0.96	0.05	-0.14	-0.52
Type-II	1	0.08	-0.12	-0.52
	0.25	-0.12	-0.17	-0.27
	1	0.09	-0.11	-0.51
Type-III	0.25	-0.12	-0.17	-0.27
	0.96	0.12	-0.07	-0.45
	1	0.16	-0.04	-0.44

^aOnly the representative surface phases are listed.

-III hydrogen adsorbed phase is more stable (by 0.04 eV/per (1×1)) than Type-I) at the stage of high potential (e.g., 0.3 V). With lowering potential, Type-I has become the dominated phase at low potential (<0.2 V). For example, the ($\Delta G_{\theta_i}(0 \text{ V})$) of Type-I 1 ML H surface is -0.52 eV per (1×1) , whereas the ΔG_{θ_i} of Type-II and -III are -0.51 and -0.44 eV per (1×1) respectively. This implies that the mixed surface phases are determined by the different types of surface based on the reaction conditions.

For the four types of surfaces (Type-I, -II, -III, and -M), we have plotted the coverage–potential, the total passed charge–potential, and CV curves in Figure 2 (see also Figures S5 and S6). The CV curves (Figure 2d–g) are derived by the differentiating total passed charge with respect to the potential; thus, each CV peak corresponds to a sharp change in the potential–coverage curve of Figure 2a. Figure 2e,f shows that the calculated CV curve has two peaks for the Type-II and -III surfaces, but three for Type-I (Figure 2d) and Type-M (Figure 2g) surfaces. We note that the value of the Pt(110) total passed charge is about $\sim 220 \mu\text{C}/\text{cm}^2$ at the lower potential end (<0.1 V), which is consistent with the typical overall total passed charge measured for the desorption of the adsorbed H layer $200\text{--}300 \mu\text{C}/\text{cm}^2$ on Pt surfaces^{14,58} (mainly due to the discharging of H to proton).

By using eqs 1–6, we can determine the coverages and CV curves for a surface domain. We first calculate those for the surface domain Type-I, -II, and -III (i.e., $t = 1, 2,$ and 3 in eqs 3–5, respectively). Next, we have taken the surface structure complexity in reality into account, where the experiment pretreatment conditions may lead to multiple domains. We therefore considered a model system, Type-M, that has equal populations for three types of domains (i.e., $c_1 = 1/3,$ $c_2 = 1/3$ and $c_3 = 1/3$ for Type-I, -II, and -III, respectively).

Now we have a close look at Figure 2. For the Type-I domain, there are roughly four plateaus (i.e., $0.4\text{--}0.36$ V, $0.33\text{--}0.22$ V, $0.20\text{--}0.16$ V, and $0.13\text{--}0$ V) in the coverage–potential curve. Each plateau is associated with a characteristic H coverage. The curve shows that the surface is already covered by H atoms at relatively high potentials (<0.40 V). At potentials near 0.33 V, the surface is dominated by 0.5 ML of H. The surface is then occupied by ~ 0.65 ML of H in between 0.20 and 0.16 V, where the Type-Ia surface transforms to Type-Ib surface by creating the Pt_{5c} site. Below 0.1 V, the H coverage grows to ~ 0.9 ML, which is similar to that on Pt(111) surface, about 1 ML at 0 V.^{57,59} The ridge (stepped) Pt sites tend to bond H more strongly than the terrace sites,

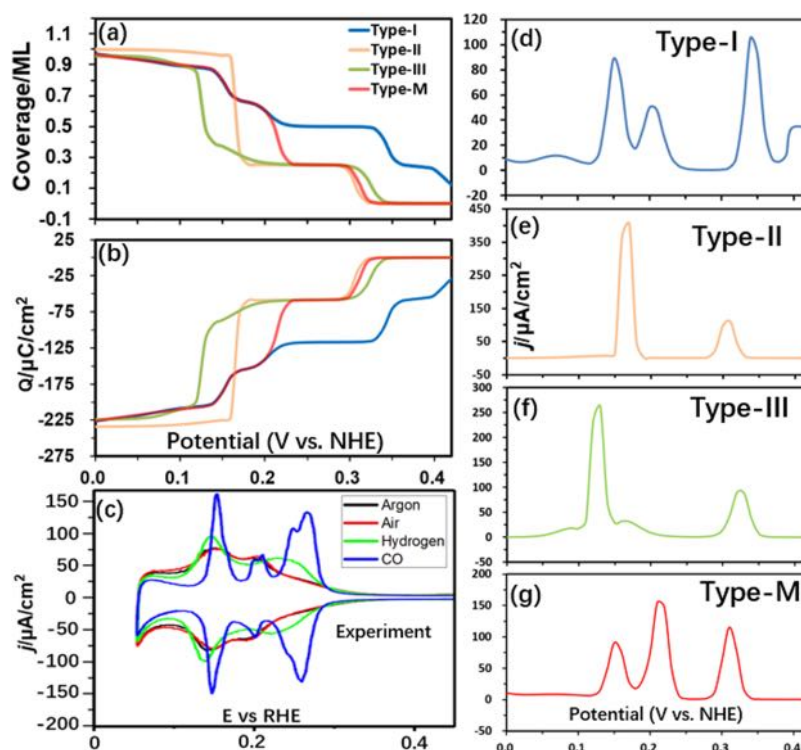


Figure 2. (a) Diagrams of the coverage vs potential, (b) total passed charge (Q) vs potential, (c) cyclic voltammetry (CV) responses of Pt(110) in 0.1 M perchloric acid cooled in different gaseous environment after flame annealing. Sweep rate = 50 mV/s. Reproduced with permission from ref 26. Copyright 2019 Elsevier, Inc. (d–g) Related CV curves for the Type-I, -II, -III, and -M surfaces.

which is in line with the observation in experiment that Pt defect sites are covered by H species even at high potential.⁶⁰

Type-I domain has three reversible electroadsorption peaks centered at 0.15, 0.20, and 0.34 V in the H_{upd} region from 0.05 to 0.4 V. These CV peaks correspond to the transition of different surface H coverage phases. For example, the 0.15 V peak is associated with average H coverage from 0.65 to 0.9 ML. The peak at 0.20 V is of interest, which reflects the Type-Ia to -Ib transformation where the average H coverage also increases from 0.5 to 0.60 ML.

For the Type-II surface, there are three plateaus at 0.4–0.32 V, 0.29–0.18 V, and 0.16–0 V (see Figure 2a). The water starts to dissociate to produce adsorbed H on surface at 0.32 V, and the coverage builds up to 0.25 ML H at 0.29 V. This coverage is maintained until 0.18 V. Below 0.16 V, a 1 ML of H overlayer is preferred thermodynamically, and this remains until 0 V. The voltammetric curve thus shows two characteristic adsorption peaks at 0.17 and 0.31 V. The peaks are related to the 0.25 and 1 ML coverage plateaus.

Similar with the Type-II domain, the Type-III domain also shows roughly three plateaus in the coverage–potential curve, which are located at 0.4–0.34 V, 0.30–0.19 V, and 0.11–0 V, respectively. The underpotential H appears as early as \sim 0.34 V, and then the domain is covered by 0.25 ML H at 0.30–0.19 V. Upon further lowering the electrochemical potential, the domain is dominated by 0.96 ML adsorbed H, which corresponds to the third phase plateau below 0.10 V. The voltammetric curve of Type-III shows two characteristic adsorption potentials, which are centered at 0.13 and 0.32 V as shown in Figure 2f. The peaks at 0.13 and 0.32 V correspond to the phase transition from 0.25 to 0.96 ML and that from 0 to 0.25 ML, respectively.

For the model surface, Type-M, the phase diagram is in fact the thermodynamics average of the contributions from the Type-I, -II, and -III surfaces domains. Figure 2a shows that the coverage–potential curve of Type-M has four plateaus at the underpotential region, which are centered at 0.4–0.33 V, 0.29–0.23 V, 0.20–0.16 V, and 0.13–0 V. The coverage at the high potential end is mainly contributed to by the Type-II domain and then taken over by the Type-I domains at lower potentials ($<$ 0.21 V). It should be emphasized that the exact position of these plateaus is much related to the assumed value of c_i that is set as 1/3 for each domain. By decreasing the proportion of Type-I surface (c_1), one can see that the plateau at \sim 0.2 V would gradually disappear (as shown in the simulated results in Figure S6).

As shown in Figures 2g and S6, the CV curves of Type-M are similar with those of Type-I with c_i being 1/3, where the peaks are centered at 0.15, 0.21, and 0.31 V. The two peaks at 0.15 and 0.21 V would gradually merge into one peak at about 0.17 V when the proportion of Type-I decreases (Figure S6). Our numerical simulation demonstrate that the CV curve is sensitive to the surface structures when there are multiple domains.

Indeed, the CV curves of Pt(110) in experiment are found to be dependent on the cooling environment.^{25,26} For comparison, we also show the experimental CV curves in Figure 2c obtained from literatures.²⁶ Obviously, our results for the Type-I surface, with three reversible electroadsorption peaks at 0.15, 0.20, and 0.34 V in the H_{upd} region, are consistent with the experimental result with the CO-cooled electrode (blue line),²⁶ where the peaks are centered at 0.145, 0.20, and 0.25 V vs RHE were observed. It should be mentioned that the peaks of the CV curve kept the same potential versus RHE at different pH values.²⁷ Attard et al. suggest that due to the strong

adsorption of CO at the ridge sites the CO-cooled electrode is dominated by (1×1) surface domain.²⁵ However, the Type-III surface, with CV peaks at 0.13 and 0.32 V, agrees with the dual peaks at 0.12 and 0.25 V in the hydrogen-cooled electrode.²⁷ The 0.25 V peak in experiment²⁶ shifts to a higher potential ~ 0.3 V relative to our calculations, which could be caused by the competitive adsorption of hydronium ion and other solute species (e.g., OH^-) as suggested by Attard^{23,25} which reduces the adsorption energy of H. The ~ 0.3 V from our calculation is in accordance with the previous theoretical calculation by Tan, where the main peak at 0.32 V is found for Pt nanoparticles.¹¹

To summarize this subsection, our results show that the three quantities, namely, the surface coverage, the total passed charge ($Q(U)$), and CV curves, are intimately correlated. By decreasing the electrochemical potential, one can increase the coverage of H on all the type surfaces in a *stepwise* manner to yield different plateaus in the potential-coverage diagram. The CV peaks can be utilized to distinguish the presence of the stepped sites (e.g., peak at 0.3 V) due to the strong adsorption of H species at the stepped sites. Interestingly, it can also be utilized to identify the surface reconstruction transition (e.g., the appearance of Pt_{sc} sites at 0.2 V).

3.2. Hydrogen Evolution Reaction. With the surface phase determined, on all surfaces the H coverage was shown to be dependent on the applied electrochemical potential: By reducing the electrochemical potential, one can gradually build up the coverage of the surface H. We are now in a position to explore the hydrogen evolution reaction (HER) at equilibrium potential, especially for the unique Pt_{sc} structure of Type-Ib surface. The initial H coverage is at the equilibrium coverage and different reaction scenarios have been considered in reaction pathway (e.g., with H vacancy or in the presence of additional adsorbed H). Typically, the highest activity occurs at the 1 ML H coverage or slightly above (e.g., 1.04 ML). In this work, we only considered the Tafel reaction mechanism ($\text{H} + \text{H} \rightarrow \text{H}_2$), which was found to be the most favorable pathway for active metals (e.g., Pt) in general.⁸

Figure 3 shows the lowest free energy pathway on Type-I, -II, and -III (Type-I is at the Type-Ib structure at 0 V), and the reaction snapshots are highlighted in Figures 3 and S7. We found that the Type-I surface has the highest HER activity with the reaction barrier (~ 0.52 eV), much lower than the other two surface domains. This is not surprising because the Pt_{sc} sites only appear in Type-I surface, which are found to be the best reaction sites for HER. The finding of Pt_{sc} as the active site is consistent with the recent work on nanoparticle, where the less-coordinated Pt (such as apex atoms at $\text{Pt}_{44}\text{H}_{80}$ octahedron) has the highest activity.^{47,61} As shown for HER at the Pt_{sc} sites, the reaction occurs by combining the top site adsorbed H with a nearby bridge H of the Pt_{sc} . At the TS, the bridging H moves to the atop site and evolve the H–H bond with the top H, where the H–H distance is 1.13 Å (see Figure 3). After the TS, the surface is left with H vacancies (MS state in Figure 3) and the subsequent Volmer step will fill the H vacancies and recover the surface. In contrast, for the Type-II and -III domains, the reaction barriers are much higher: 0.86 and 0.69 eV, respectively. These high barriers are consistent with the previous calculations, where the Tafel reaction barrier on Pt(110)- (1×2) surface is found to be 0.75 eV at 1 ML H coverage.⁴⁶ The Tafel reaction occurs through the coupling between two bridging adsorbed H atoms. At the TSs, both H atoms are also activated to the atop site on the same Pt atom to

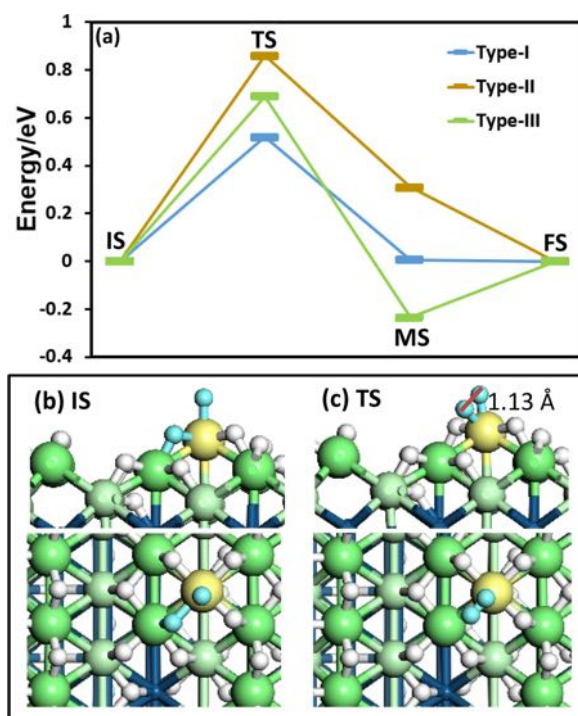


Figure 3. (a) free energy profile via Tafel pathway on Type-I, -II, and -III surfaces at equilibrium potential. Located IS (b), TS (c) for Type-I surface are also shown. The labeled distances are in angstroms. Large ball: Pt atoms; small white ball: H atoms; small cyan ball: H atoms in reaction.

produce H_2 (see Figure S7), where the H–H distance is around 1.19 Å. By comparing the HER reaction on different surface domains, we can conclude that the high activity of Type-I domain is associated with the initial presence of the top site adsorbed H, which is already activated to react with the nearby H. The low-coordinated Pt_{sc} created by the surface reconstruction is the key to stabilize the top site H.

$$j = AFS^{-1}SN_A^{-1} e^{-\Delta G/RT} [\text{site}] \quad (8)$$

By using microkinetics, we have further deduced the reaction current (j) of hydrogen evolution on different surface domains based on eq 8, where A is the pre-exponential factor (it is set as 10^{13} at 300 K), S is the total surface area, and $[\text{site}]$ is the concentration of the reactive site (ML). We found that the currents at the equilibrium potential are 1.5×10^{-2} , 2.9×10^{-9} , and 2.1×10^{-5} A/cm² for the Type-I, -II, and -III surface domains, respectively. We note that our estimated activity of Type-I surface is slightly larger than the equilibrium current j_0 deduced from experiment (0.98 mA/cm²),⁸ implying that the population of Type-I domain is less than 7% in experiment.

It should be mentioned that we have separated the slow and fast steps in treating the HER system, and on the basis of this, we obtained the H coverage in the grand canonical ensemble. This requires that the Volmer step, the charging/discharging of solution H_3O^+ to H^* , is sufficiently fast compared to H_2 evolution reactions, which was also assumed in many previous works by other groups and us.^{39,57,59} When HER occurs, the above thermodynamics equilibrium may break, particularly at the high current conditions, when the Volmer step becomes rate-limiting. This typically occurs at the high overpotentials (e.g., below -0.2 V vs NHE), which is not the concern of this work. In fact, under the low-overpotential conditions, the HER

on Pt typically has the Tafel slope of 30 mV/dec,⁸ which is consistent with our model that the Volmer step is fast, and the rate-determining step is the H–H coupling following the Tafel mechanism.

3.3. Formation Mechanism of Pt_{5c} Sites under Electrochemical Conditions. For the importance of the Pt_{5c} site in HER, we are now in a position to understand how these Pt_{5c} sites are created under electrochemical conditions. Since the phase diagram already shows the thermodynamics that the Type-Ib is more stable than Type-Ia at low potential (<0.2 V), where the average H coverage is higher than 0.60 ML. By using SSW-NN simulation, we have first extensively explored the likely pathways from Type-Ia to -Ib at about 0.2 V. The lowest energy pathway determined is shown in Figure 4, together with the key reaction snapshots at 0.67 ML H coverage (the structures along the whole pathway are shown in Figure S8).

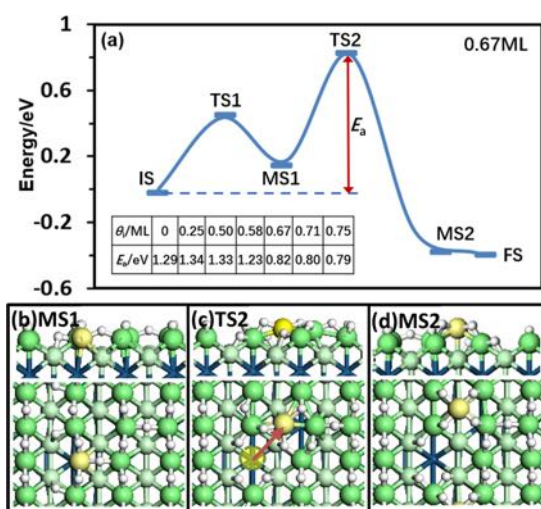


Figure 4. Energy profile for Pt_{5c} formation at 0.67 ML H of Type-I surface (a) and the optimized structures of intermediate states (b–d). For the optimized structures: large green ball: surface bridge Pt atoms; large pale green ball: surface terrace Pt atoms; large yellow ball: five-coordinated Pt; small white ball: H atoms.

The reconstruction reaction can be divided into three elementary steps with an overall barrier 0.82 eV at the H coverage of 0.67 ML, suggesting the reaction is able to occur at the ambient temperatures. In this pathway, the final Pt_{5c} concentration is 0.04 ML, one Pt_{5c} per Pt(110)-p(3 × 4). After one Pt_{5c} forms per Pt(110)-p(3 × 4), the subsequent pathways to form more Pt_{5c} sites are found to be kinetically unfavorable, being at least 1.0 eV (see Figure S9).

The three steps of Pt_{5c} formation contain two H-rearrangement steps, IS to MS1 and MS2 to FS, and one Pt-migration step, MS1 to MS2 (see Figure 4). The reaction starts by the accumulation of surface adsorbed H over one row of ridge Pt atoms (state MS1, Figure 4). The first transition state (TS1) occurs when the surface H move across from one row of bridge Pt atoms to another. The reactive ridge Pt (yellow atom, Figure 4) atoms are pushed outward above the surface plane due to the adsorbed H atoms (2.81–3.06 Å). This Pt atom then undergoes the migration to the neighbor valley (red arrow in state TS2, Figure 4). In the step, the moving Pt carries two H atoms and start to coordinate with the other row of ridge Pt atoms. There are three Pt–Pt bonds breaking and one Pt–H

bond breaking for the Pt to move out from its original position (see Figure 4, TS2). In the final state, after the Pt_{5c} forms, the H in the valley tends to accumulate around the Pt_{5c} site (from site 1 (S1) to site 2 (S2) in Figure S8, MS2) to reach a local high H coverage.

By focusing on the Pt-migration step, we have evaluated the reaction barrier at different H coverage (θ_i) conditions, namely, 0, 0.25, 0.50, 0.58, 0.71, and 0.75 ML. The reaction barriers obtained are listed in the inset table in Figure 4a, and the detailed TS geometries are shown in Figure S10. Indeed, we found that the reaction barriers (E_a) of Pt-migration decreases rapidly with the increase of coverage. Below a H coverage of 0.5 ML, which corresponds to a voltage above 0.35 V (see Figure 2), the reaction barrier is substantially high, being above 1.2 eV. Above 0.67 ML of H coverage (below 0.2 V), the barrier reaches to a rather constant value of 0.8 eV. In fact, this phenomenon can be explained from the TS geometry, where only above 0.67 ML is the migrating Pt reactive center capped with adsorbed H atoms. Obviously, the migrating Pt that is adsorbed by H can be better stabilized at the TS, which helps to reduce the original Pt–Pt bonding by compensating with the additional Pt–H bonding.

It should be mentioned that we have also examined the possible effect of the surface excess charge on the reaction barrier for Pt_{5c} formation on three different coverages. The charged-slab DFT/CM-MPB method developed previously are utilized to add explicit charge onto the surface to evaluate charge effect on the reaction barrier.^{45,53} As shown in Figure S11, we found that the excess surface charge plays only a minor role on influencing the reaction barrier, where the magnitude is below 0.08 eV per charge. Our results are consistent with the recent theoretical studies, showing that the barrier for Pt lifting is only slightly affected by electric fields.⁶²

4. CONCLUSION

This work represents the first theoretical attempt to elucidate the *in situ* surface condition of Pt(110) electrode under electrochemical conditions. We have calculated the coverage, total passed charge, and CV curves of four types of Pt(110) surfaces identified from SSW-NN simulation. The Type-I surface shows four plateaus on its phase diagram and three CV peaks centered at 0.15, 0.20, and 0.34 V. Importantly, Type-I surface can undergo a facile reconstruction from Type-Ia to -Ib at 0.60 ML average hydrogen coverage around 0.2 V, which produces five-coordinated Pt_{5c} sites. The Type-II and -III structures have three plateaus on their coverage–potential curves and only two CV peaks. These results explain the observed CV curve difference for the Pt(110) electrode under H₂ and CO treatment conditions.

Our reaction pathways for HER at different surfaces further demonstrate that the Pt_{5c} sites have the highest activity for HER, where the Tafel reaction barrier is only 0.52 eV at equilibrium potential. The thermodynamic and kinetic results for Pt(110) reconstruction provide atomic-level information on how the metal electrode evolves under electrochemical conditions and how the catalytic activity varies upon the change of surface structure and the applied potential. This detailed knowledge may benefit the rational design of better electrode materials in the future.

■ ASSOCIATED CONTENT

SI Supporting Information

The Supporting Information is available free of charge at <https://pubs.acs.org/doi/10.1021/acs.jpcc.1c02222>.

Theoretical methods and calculation details, the surface structures and related properties of Pt(110) surfaces, and XYZ coordinates for the configurations in [Figure 1 \(PDF\)](#)

■ AUTHOR INFORMATION

Corresponding Authors

Ya-Hui Fang – School of Chemical and Environmental Engineering, Shanghai Institute of Technology, Shanghai 201418, China; orcid.org/0000-0001-5533-4962; Email: huihuifang@sit.edu.cn

Zhi-Pan Liu – Collaborative Innovation Center of Chemistry for Energy Material, Shanghai Key Laboratory of Molecular Catalysis and Innovative Materials, Key Laboratory of Computational Physical Science (Ministry of Education), Department of Chemistry, Fudan University, Shanghai 200433, China; orcid.org/0000-0002-2906-5217; Email: zpliu@fudan.edu.cn

Authors

Dan-dan Song – School of Chemical and Environmental Engineering, Shanghai Institute of Technology, Shanghai 201418, China

Hui-xia Li – School of Chemical and Environmental Engineering, Shanghai Institute of Technology, Shanghai 201418, China

Complete contact information is available at: <https://pubs.acs.org/doi/10.1021/acs.jpcc.1c02222>

Notes

The authors declare no competing financial interest.

■ ACKNOWLEDGMENTS

This work was supported by National Key Research and Development Program of China (2018YFA0208600), National Science Foundation of China (22033003, 21573149, 21533001, 91745201), and Shanghai “ChenGuang” project (13CG61).

■ REFERENCES

- (1) Bruix, A.; Margraf, J. T.; Andersen, M.; Reuter, K. First-principles-based multiscale modelling of heterogeneous catalysis. *Nat. Catal.* **2019**, *2*, 659–670.
- (2) Zhu, J.; Hu, L.; Zhao, P.; Lee, L. Y. S.; Wong, K.-Y. Recent Advances in Electrocatalytic Hydrogen Evolution Using Nanoparticles. *Chem. Rev.* **2020**, *120*, 851–918.
- (3) Stamenkovic, V. R.; Strmcnik, D.; Lopes, P. P.; Markovic, N. M. Energy and fuels from electrochemical interfaces. *Nat. Mater.* **2017**, *16*, 57–69.
- (4) Stamenkovic, V. R.; Mun, B. S.; Mayrhofer, K. J. J.; Ross, P. N.; Markovic, N. M. Effect of surface composition on electronic structure, stability, and electrocatalytic properties of Pt-transition metal alloys: Pt-skin versus Pt-skeleton surfaces. *J. Am. Chem. Soc.* **2006**, *128*, 8813–8819.
- (5) Tian, N.; Zhou, Z. Y.; Sun, S. G.; Ding, Y.; Wang, Z. L. Synthesis of tetrahedral platinum nanocrystals with high-index facets and high electro-oxidation activity. *Science* **2007**, *316*, 732–735.
- (6) Greeley, J.; Jaramillo, T. F.; Bonde, J.; Chorkendorff, I. B.; Norskov, J. K. Computational high-throughput screening of electrocatalytic materials for hydrogen evolution. *Nat. Mater.* **2006**, *5*, 909–13.
- (7) Ji, L.; Wang, J.; Zuo, S.; Chen, Z. In Situ Preparation of Pt Nanoparticles Supported on N-Doped Carbon as Highly Efficient Electrocatalysts for Hydrogen Production. *J. Phys. Chem. C* **2017**, *121*, 8923–8930.
- (8) Markovic, N. M.; Grgur, B. N.; Ross, P. N. Temperature-dependent hydrogen electrochemistry on platinum low-index single-crystal surfaces in acid solutions. *J. Phys. Chem. B* **1997**, *101*, 5405–5413.
- (9) Clavilier, J.; Albalat, R.; Gomez, R.; Orts, J. M.; Feliu, J. M.; Aldaz, A. Study of the Charge Displacement at Constant Potential during Co Adsorption on Pt(110) and Pt(111) Electrodes in Contact with a Perchloric-Acid Solution. *J. Electroanal. Chem.* **1992**, *330*, 489–497.
- (10) Conway, B. E.; Tilak, B. V. Interfacial processes involving electrocatalytic evolution and oxidation of H₂, and the role of chemisorbed H. *Electrochim. Acta* **2002**, *47*, 3571–3594.
- (11) Tan, T. L.; Wang, L. L.; Zhang, J.; Johnson, D. D.; Bai, K. W. Platinum Nanoparticle During Electrochemical Hydrogen Evolution: Adsorbate Distribution, Active Reaction Species, and Size Effect. *ACS Catal.* **2015**, *5*, 2376–2383.
- (12) Kortlever, R.; Peters, I.; Koper, S.; Koper, M. T. M. Electrochemical CO₂ Reduction to Formic Acid at Low Overpotential and with High Faradaic Efficiency on Carbon-Supported Bimetallic Pd-Pt Nanoparticles. *ACS Catal.* **2015**, *5*, 3916–3923.
- (13) Gao, D.; Wang, J.; Wu, H.; Jiang, X.; Miao, S.; Wang, G.; Bao, X. pH effect on electrocatalytic reduction of CO₂ over Pd and Pt nanoparticles. *Electrochem. Commun.* **2015**, *55*, 1–5.
- (14) Markovića, N. M.; Sarraf, S. T.; Gasteiger, H. A.; Ross, P. N. Hydrogen electrochemistry on platinum low-index single-crystal surfaces in alkaline solution. *J. Chem. Soc., Faraday Trans.* **1996**, *92*, 3719–3725.
- (15) Schmidt, T. J.; Ross, P. N.; Markovic, N. M. Temperature dependent surface electrochemistry on Pt single crystals in alkaline electrolytes Part 2. The hydrogen evolution/oxidation reaction. *J. Electroanal. Chem.* **2002**, *524*, 252–260.
- (16) Barber, J. H.; Conway, B. E. Structural specificity of the kinetics of the hydrogen evolution reaction on the low-index surfaces of Pt single-crystal electrodes in 0.5 M dm⁻³ NaOH. *J. Electroanal. Chem.* **1999**, *461*, 80–89.
- (17) Conway, B. E.; Barber, J.; Morin, S. Comparative evaluation of surface structure specificity of kinetics of UPD and OPD of H on single-crystal Pt electrodes. *Electrochim. Acta* **1998**, *44*, 1109–1125.
- (18) Subbaraman, R.; Tripkovic, D.; Strmcnik, D.; Chang, K. C.; Uchimura, M.; Paulikas, A. P.; Stamenkovic, V.; Markovic, N. M. Enhancing Hydrogen Evolution Activity in Water Splitting by Tailoring Li(+)-Ni(OH)₂-Pt Interfaces. *Science* **2011**, *334*, 1256–1260.
- (19) Hoshi, N.; Nakamura, M.; Sakata, O.; Nakahara, A.; Naito, K.; Ogata, H. Surface X-ray Scattering of Stepped Surfaces of Platinum in an Electrochemical Environment: Pt(331)=3(111)-(111) and Pt(511)=3(100)-(111). *Langmuir* **2011**, *27*, 4236–4242.
- (20) García-Arárez, N.; Climent, V.; Herrero, E.; Feliu, J. M. On the electrochemical behavior of the Pt(100) vicinal surfaces in bromide solutions. *Surf. Sci.* **2004**, *560*, 269–284.
- (21) Minca, M.; Penner, S.; Loerting, T.; Menzel, A.; Bertel, E.; Zucca, R.; Redinger, J. Chemisorption of hydrogen on the missing-row Pt(110)-(1 × 2) surface. *Top. Catal.* **2007**, *46*, 161–167.
- (22) Souza-Garcia, J.; Climent, V.; Feliu, J. M. Voltammetric characterization of stepped platinum single crystal surfaces vicinal to the (110) pole. *Electrochem. Commun.* **2009**, *11*, 1515–1518.
- (23) Attard, G. A.; Brew, A. Cyclic voltammetry and oxygen reduction activity of the Pt{110}-(1 × 1) surface. *J. Electroanal. Chem.* **2015**, *747*, 123–129.
- (24) Rodriguez, P.; Garcia, G.; Herrero, E.; Feliu, J. M.; Koper, M. T. M. Effect of the Surface Structure of Pt(100) and Pt(110) on the Oxidation of Carbon Monoxide in Alkaline Solution: an FTIR and Electrochemical Study. *Electrocatalysis* **2011**, *2*, 242–253.
- (25) Attard, G. A.; Hunter, K.; Wright, E.; Sharman, J.; Martinez-Hincapie, R.; Feliu, J. M. The voltammetry of surfaces vicinal to

- Pt{110}: Structural complexity simplified by CO cooling. *J. Electroanal. Chem.* **2017**, *793*, 137–146.
- (26) Attard, G. A.; Souza-Garcia, J.; Martinez-Hincapie, R.; Feliu, J. M. Nitrate anion reduction in aqueous perchloric acid as an electrochemical probe of Pt{110}-(1 × 1) terrace sites. *J. Catal.* **2019**, *378*, 238–247.
- (27) Taguchi, S.; Feliu, J. M. Electrochemical reduction of nitrate on Pt(S) n(111) x(111) electrodes in perchloric acid solution. *Electrochim. Acta* **2007**, *52*, 6023–6033.
- (28) Souza-Garcia, J.; Angelucci, C. A.; Climent, V.; Feliu, J. M. Electrochemical features of Pt(S) n(110) x(100) surfaces in acidic media. *Electrochem. Commun.* **2013**, *34*, 291–294.
- (29) Hoshi, N.; Asaumi, Y.; Nakamura, M.; Mikita, K.; Kajiwara, R. Structural Effects on the Hydrogen Oxidation Reaction on n(111)-(111) Surfaces of Platinum. *J. Phys. Chem. C* **2009**, *113*, 16843–16846.
- (30) Kajiwara, R.; Asaumi, Y.; Nakamura, M.; Hoshi, N. Active sites for the hydrogen oxidation and the hydrogen evolution reactions on the high index planes of Pt. *J. Electroanal. Chem.* **2011**, *657*, 61–65.
- (31) Nakamura, M.; Kobayashi, T.; Hoshi, N. Structural dependence of intermediate species for the hydrogen evolution reaction on single crystal electrodes of Pt. *Surf. Sci.* **2011**, *605*, 1462–1465.
- (32) Rao, C. V.; Viswanathan, B. Monodispersed Platinum Nanoparticle Supported Carbon Electrodes for Hydrogen Oxidation and Oxygen Reduction in Proton Exchange Membrane Fuel Cells. *J. Phys. Chem. C* **2010**, *114*, 8661–8667.
- (33) Babic, B. M.; Vracar, L. M.; Radmilovic, V.; Krstajic, N. V. Carbon cryogel as support of platinum nano-sized electrocatalyst for the hydrogen oxidation reaction. *Electrochim. Acta* **2006**, *51*, 3820–3826.
- (34) Zhou, M.; Bao, S. J.; Bard, A. J. Probing Size and Substrate Effects on the Hydrogen Evolution Reaction by Single Isolated Pt Atoms, Atomic Clusters, and Nanoparticles. *J. Am. Chem. Soc.* **2019**, *141*, 7327–7332.
- (35) Bjorketun, M. E.; Bondarenko, A. S.; Abrams, B. L.; Chorkendorff, I.; Rossmeisl, J. Screening of electrocatalytic materials for hydrogen evolution. *Phys. Chem. Chem. Phys.* **2010**, *12*, 10536–10541.
- (36) Hamada, I.; Morikawa, Y. Density-functional analysis of hydrogen on Pt(111): Electric field, solvent, and coverage effects. *J. Phys. Chem. C* **2008**, *112*, 10889–10898.
- (37) Cai, Y.; Anderson, A. B.; Angus, J. C.; Kostadinov, L. N. Hydrogen evolution on diamond electrodes by the volmer-Heyrovsky mechanism. *J. Electrochem. Soc.* **2007**, *154*, F36–F43.
- (38) Ishikawa, Y.; Mateo, J. J.; Tryk, D. A.; Cabrera, C. R. Direct molecular dynamics and density-functional theoretical study of the electrochemical hydrogen oxidation reaction and underpotential deposition of H on Pt(111). *J. Electroanal. Chem.* **2007**, *607*, 37–46.
- (39) Santana, J. A.; Mateo, J. J.; Ishikawa, Y. Electrochemical Hydrogen Oxidation on Pt(110): A Combined Direct Molecular Dynamics/Density Functional Theory Study. *J. Phys. Chem. C* **2010**, *114*, 4995–5002.
- (40) Santos, E.; Hindelang, P.; Quaino, P.; Schmickler, W. A model for the Heyrovsky reaction as the second step in hydrogen evolution. *Phys. Chem. Chem. Phys.* **2011**, *13*, 6992.
- (41) Bhardwaj, M.; Balasubramanian, R. A new method for determining kinetic parameters by simultaneously considering all the independent conditions at an overpotential. in case of hydrogen evolution reaction following Volmer-Heyrovsky-Tafel mechanism. *Int. J. Hydrogen Energy* **2008**, *33*, 248–251.
- (42) Skulason, E.; Karlberg, G. S.; Rossmeisl, J.; Bligaard, T.; Greeley, J.; Jonsson, H.; Norskov, J. K. Density functional theory calculations for the hydrogen evolution reaction in an electrochemical double layer on the Pt(111) electrode. *Phys. Chem. Chem. Phys.* **2007**, *9*, 3241–3250.
- (43) Skulason, E.; Tripkovic, V.; Bjorketun, M. E.; Gudmundsdottir, S.; Karlberg, G.; Rossmeisl, J.; Bligaard, T.; Jonsson, H.; Norskov, J. K. Modeling the Electrochemical Hydrogen Oxidation and Evolution Reactions on the Basis of Density Functional Theory Calculations. *J. Phys. Chem. C* **2010**, *114*, 18182–18197.
- (44) Santos, E.; Hindelang, P.; Quaino, P.; Schulz, E. N.; Soldano, G.; Schmickler, W. Hydrogen Electrocatalysis on Single Crystals and on Nanostructured Electrodes. *ChemPhysChem* **2011**, *12*, 2274–2279.
- (45) Fang, Y.-H.; Wei, G.-F.; Liu, Z.-P. Catalytic Role of Minority Species and Minority Sites for Electrochemical Hydrogen Evolution on Metals: Surface Charging, Coverage, and Tafel Kinetics. *J. Phys. Chem. C* **2013**, *117*, 7669–7680.
- (46) Van den Bossche, M.; Skulason, E.; Rose-Petruck, C.; Jónsson, H. Assessment of Constant-Potential Implicit Solvation Calculations of Electrochemical Energy Barriers for H₂ Evolution on Pt. *J. Phys. Chem. C* **2019**, *123*, 4116–4124.
- (47) Wei, G. F.; Liu, Z. P. Restructuring and Hydrogen Evolution on Pt Nanoparticle. *Chem. Sci.* **2015**, *6*, 1485–1490.
- (48) Huang, S. D.; Shang, C.; Zhang, X. J.; Liu, Z.-P. Material Discovery by Combining Stochastic Surface Walking Global Optimization with a Neural Network. *Chem. Sci.* **2017**, *8*, 6327–6337.
- (49) Ma, S.; Huang, S. D.; Fang, Y. H.; Liu, Z. P. TiH Hydride Formed on Amorphous Black Titania: Unprecedented Active Species for Photocatalytic Hydrogen Evolution. *ACS Catal.* **2018**, *8*, 9711–9721.
- (50) Shang, C.; Huang, S. D.; Liu, Z. P. Massively Parallelization Strategy for Material Simulation using High-Dimensional Neural Network Potential. *J. Comput. Chem.* **2019**, *40*, 1091–1096.
- (51) Zhou, L.; Zhou, X. F.; Huang, X. D.; Liu, Z. P.; Zhao, D. Y.; Yao, X. D.; Yu, C. Z. Designed synthesis of LiMn₂O₄ microspheres with adjustable hollow structures for lithium-ion battery applications. *J. Mater. Chem. A* **2013**, *1*, 837–842.
- (52) Fang, Y. H.; Ma, S. C.; Liu, Z. P. 3-D Tunnel TiO₂ Crystal Phase as a Fast Charging Lithium Battery Anode from Stochastic Surface Walking-Based Material Screening. *J. Phys. Chem. C* **2019**, *123*, 19347–19353.
- (53) Fang, Y. H.; Liu, Z. P. Mechanism and Tafel Lines of Electro-Oxidation of Water to Oxygen on RuO₂(110). *J. Am. Chem. Soc.* **2010**, *132*, 18214–18222.
- (54) Shang, C.; Liu, Z. P. Origin and Activity of Gold Nanoparticles as Aerobic Oxidation Catalysts in Aqueous Solution. *J. Am. Chem. Soc.* **2011**, *133*, 9938–9947.
- (55) Li, Y. F.; Liu, Z. P.; Liu, L. L.; Gao, W. G. Mechanism and Activity of Photocatalytic Oxygen Evolution on Titania Anatase in Aqueous Surroundings. *J. Am. Chem. Soc.* **2010**, *132*, 13008–13015.
- (56) Rossmeisl, J.; Qu, Z. W.; Zhu, H.; Kroes, G. J.; Norskov, J. K. Electrolysis of water on oxide surfaces. *J. Electroanal. Chem.* **2007**, *607*, 83–89.
- (57) Karlberg, G. S.; Jaramillo, T. F.; Skulason, E.; Rossmeisl, J.; Bligaard, T.; Norskov, J. K. Cyclic voltammograms for H on Pt(111) and Pt(100) from first principles. *Phys. Rev. Lett.* **2007**, *99*, 126101.
- (58) Hitotsuyanagi, A.; Nakamura, M.; Hoshi, N. Structural effects on the activity for the oxygen reduction reaction on n(111)-(100) series of Pt: correlation with the oxide film formation. *Electrochim. Acta* **2012**, *82*, 512–516.
- (59) Tan, T. L.; Wang, L.-L.; Johnson, D. D.; Bai, K. Hydrogen Deposition on Pt(111) during Electrochemical Hydrogen Evolution from a First-Principles Multiadsorption-Site Study. *J. Phys. Chem. C* **2013**, *117*, 22696–22704.
- (60) Strmcnik, D.; Tripkovic, D.; van der Vliet, D.; Stamenkovic, V.; Markovic, N. M. Adsorption of hydrogen on Pt(111) and Pt(100) surfaces and its role in the HOR. *Electrochem. Commun.* **2008**, *10*, 1602–1605.
- (61) Gu, G. H.; Lim, J.; Wan, C.; Cheng, T.; Pu, H.; Kim, S.; Noh, J.; Choi, C.; Kim, J.; Goddard, W. A.; et al. Autobifunctional Mechanism of Jagged Pt Nanowires for Hydrogen Evolution Kinetics via End-to-End Simulation. *J. Am. Chem. Soc.* **2021**, *143*, 5355–5363.
- (62) Fang, Y. H.; Liu, Z. P. Toward Anticorrosion Electrodes: Site-Selectivity and Self-Acceleration in the Electrochemical Corrosion of Platinum. *J. Phys. Chem. C* **2010**, *114*, 4057–4062.